AIAA JOURNAL
Vol. 34, No. 1, January 1996

Improving Curved Subsonic Diffuser Performance with Vortex Generators

B. A. Reichert*
Kansas State University, Manhattan, Kansas 66506-5106
and
B. J. Wendt†
Modern Technologies Corporation, Middleburg Heights, Ohio 44130

The objective of this research was to use vortex generators to reduce total pressure distortion (i.e., total pressure nonuniformity) and improve total pressure recovery within a curved subsonic diffuser. In this study more than 20 configurations of both co- and counter-rotating arrays of vortex generators were tested in a diffusing S duct. Surface static pressure, surface flow visualization, and exit plane total pressure and transverse velocity data were acquired. The aerodynamic performance of each configuration was assessed by calculating total pressure recovery and spatial distortion elements. The best configuration tested reduced distortion by more than 50% while improving total pressure recovery by 0.5%. The results indicate that the mechanism responsible for improved aerodynamic performance is not boundary-layer re-energization from shed axial vortices but rather the suppression of detrimental secondary flows by redirecting the flow.

Nomenclature

Cp	= static pressure coefficient
Cp_0	= total pressure coefficient
D	= duct diameter
h	= vortex generator height
l	= vortex generator lateral spacing
N	= number of vortex generators
p	= static pressure
p_0	= total pressure
$\overline{p_0}$	= average total pressure
r	= radial coordinate
s	= distance along duct centerline
x, y, z	= Cartesian coordinates
$\Delta pc/p$	= circumferential distortion intensity element
$\Delta pr/p$	= radial distortion intensity element
δ	= boundary-layer thickness, 95%
θ^-	= circumferential distortion angular extent element
ϕ	= polar coordinate

Subscripts

face	= area-weighted face average
low	= average over ϕ for constant r in regions where p_0 is less than $\overline{p_0}_{,\text{ring}}$; see Fig. 3
ref	= reference conditions at $s/D_1 = -0.5$
ring	= average over ϕ for constant r; see Fig. 3
1, 2	= inlet and exit of duct at $s/D_1 = 0$ and 5.23

Introduction

DIFFUSING S ducts are representative of curved subsonic diffusers and are characterized by the S-shaped curvature of the duct's centerline and their increasing cross-sectional area. For aircraft inlet applications the measure of duct aerodynamic performance is the ability to decelerate the flow to the desired velocity while maintaining high total pressure recovery and flow uniformity. Reduced total pressure recovery lowers propulsion efficiency, whereas nonuniform flow conditions at the engine face lower engine stall and surge limits.

The fluid dynamics of the diffusing S duct used in this study was reported by Vakili et al.[1] and Wellborn et al.[2] Strong cross-stream pressure gradients are developed by the duct's centerline curvature. Within the boundary layer this imparts a transverse or crossflow velocity that develops into counter-rotating axial vortices at the duct exit plane. These vortices are referred to as the naturally occurring vortices, since they are present in the flow without any vortex generators. Additionally, a region of boundary-layer separation was observed along the inside radius near the end of the first duct bend. We use the topological definition of separation that requires a flow whose surface visualization contains singular points (e.g., spiral nodes and saddle points). This definition is consistent with the term global separation[3] and is meant to be distinguished from a local or crossflow separation[4] where no singular points are observed in surface flow visualization.

The relationship between duct centerline curvature and increasing cross-sectional area and the resulting fluid mechanics can be understood if their effects are considered separately. In an earlier study, Vakili et al.[5] explored flow in a nondiffusing S duct that was geometrically similar in all regards to the duct used in the present study except the cross-sectional area was constant. The flowfield at the nondiffusing S-duct exit was quite similar to that of the diffusing S duct in that both are dominated by naturally occurring vortices. However, there was no boundary layer-separation in the nondiffusing S duct. This suggests that the naturally occurring vortices and resulting flow distortion originate from secondary flows caused by streamline curvature and not from boundary-layer separation. There has not been a study of a straight diffuser with the same cross-sectional area distribution as the diffusing S duct, but the average half-angle of such a diffuser would be 2.5 deg and the maximum half-angle would be 3.8 deg. Using the results of Kline et al.[6] as a guide, it is safe to assume that the flow in such a straight diffuser would not separate. Therefore, the flow separation in the diffusing S duct does not result from increasing cross-sectional area alone. Both of these conclusions indicate that detrimental secondary flows resulting from centerline curvature are responsible for the naturally occurring vortices and contribute to boundary-layer separation.

The concept of using vortex generators to reduce or eliminate boundary-layer separation has been known for many years. Early

Received Sept. 12, 1994; revision received July 31, 1995; accepted for publication July 31, 1995.

*Assistant Professor, Department of Mechanical Engineering. Senior Member AIAA.

†Research Engineer, 7530 Lucerne Drive, Islander Two, Suite 100. Member AIAA.

studies of vortex generators have focused on improving total pressure recovery in diffusers. Substantial improvements in total pressure recovery were reported by Taylor[7] and Brown[8] on various subsonic diffuser geometries. Studies of a mixed-compression inlet by Mitchell and Davis [9] and the Boeing 727 center inlet by Kaldschmidt et al.[10] established the principle of using vortex generator arrays as a means of reducing flow distortion.

Recent work on improving the performance of diffusing S ducts have considered several approaches. In another study by Vakili et al.[11] an array of blade type vortex generators, set to produce counter-rotating axial vortices, was used to prevent separation in the duct. Improvements in the total pressure recovery and total pressure uniformity at the duct exit were reported. Their use of a flow control rail device, spanning approximately half of the duct inlet circumference, was not as successful. In the report of Weng and Guo[12] a blade-shaped spoiler divides the inlet cross section of a diffusing rectangular S duct. At small angles of attack the spoiler reduces the strength of the counter-rotating vortices observed at the duct exit.

The objectives of this study were to reduce flow distortion and improve total pressure recovery in the diffusing S duct using vortex generators. Both wishbone and tapered-fin type vortex generators were tested to explore the effects of varying the number, orientation, size, lateral spacing, and axial location of vortex generators within the S duct. The data acquired for each configuration include surface static pressure, surface flow visualization, and exit plane total pressure and transverse velocity. These results were initially reported in Refs. 13 and 14. Since then, additional tests and analyses have been conducted. In total, more than 20 vortex generator configurations were studied.

This article reports the effectiveness of various vortex generator configurations by calculating total pressure recovery and spatial distortion elements from the experimental data and comparing them to values for other configurations and for the bare duct. Space limitations restrict the data contained in this article to a fraction of all of the measurements for each vortex generator configuration tested. The reader is referred to Refs. 13 and 14 for additional information. An overall concept regarding the application of vortex generators that combines knowledge of S-duct fluid mechanics with observations of the effect of each vortex generator parameter is presented. The results of this study should provide guidance to effectively utilize vortex generators to improve the aerodynamic performance of diffusing S ducts and similar curved subsonic diffusers.

Experimental Facilities and Procedures

Diffusing S Duct

The geometry of the diffusing S duct examined in this study is shown in Fig. 1. This duct is geometrically similar to the duct tested in Ref. 1 and is identical to the duct studied in Ref. 2. The duct centerline is defined by two circular arcs that lie within the xz plane as shown in Fig. 1. The cross-sectional shape of the duct perpendicular to the centerline is circular. The duct shape was chosen to facilitate both fabrication and computational fluid dynamics (CFD) analysis. When discussing locations within the duct, axial location will refer to distance to cross-stream planes measured along the duct centerline and normalized by the duct inlet diameter s/D_1. Position within cross-stream planes is specified by the polar angle ϕ, measured from the vertical in a positive clockwise direction as shown in Fig. 1, and the radial distance from the centerline r. The diameter of the cross section varies with the axial location and is given by Eq. (1)

$$\frac{D}{D_1} = 1 + 3\left(\frac{D_2}{D_1} - 1\right)\left(\frac{s/D_1}{5.23}\right)^2 - 2\left(\frac{D_2}{D_1} - 1\right)\left(\frac{s/D_1}{5.23}\right)^3 \quad (1)$$

The exit-to-inlet area ratio of the duct is 1.52, the offset of the duct resulting from the centerline curvature is $1.34D_1$, and the length of the duct measured along the centerline is $5.23D_1$.

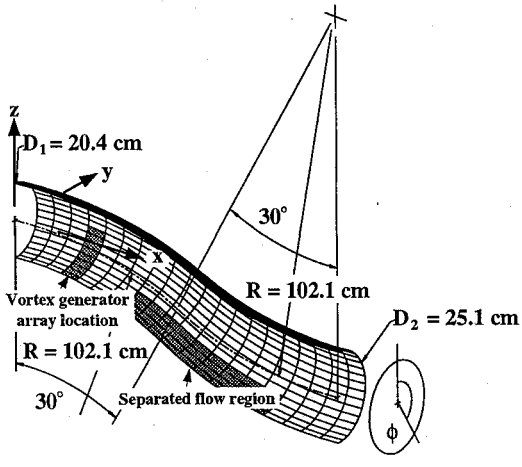

Fig. 1 Geometry of the diffusing S duct.

Facility Flow Conditions

The tests were conducted at the NASA Lewis Research Center using the Internal Fluid Mechanics Facility. Air was supplied from the test cell to a large settling chamber containing honeycomb and screens and an axisymmetric contraction having an area ratio of 59:1. Smooth circular pipes of appropriate diameter were attached upstream and downstream of the S duct to provide a uniform incoming flow and a smooth, continuous condition for flow exiting the duct. The lengths of the upstream and downstream pipes were each $3.75D_1$. After passing through the S duct, the flow was exhausted into a discharge plenum that was continuously evacuated by central exhauster facilities. The duct inlet Mach number was 0.6 for all tests. The inlet boundary-layer thickness δ_{ref} was approximately 4% of the duct inlet diameter and fully turbulent. The Reynolds number, based on inlet diameter, was approximately 2.6×10^6. Stagnation pressure and temperature were nominally test cell ambient values, 101 KPa and 298 K. Test conditions were established by regulating a control valve located between the discharge plenum and the central exhauster facilities. The flow was choked at the control valve, assuring continuous stable test conditions, unaffected by small pressure variations in the central exhauster equipment. A complete description of the Internal Fluid Mechanics Facility is given by Porro et al.[15]

Measurement Techniques

The primary set of measurements consist of exit plane surveys of the mean three-dimensional velocity field and total pressure. These were acquired by a rake probe consisting of 10 independently calibrated five-hole probe tips. The rake probe was traversed circumferentially and radially to acquire data at 720 uniformly spaced locations in the S-duct exit measurement plane. The radial spacing of measurements was 6.35 mm, and the circumferential spacing was 10 deg. The exit measurement plane is located at $s/D_1 = 5.73$. More information on the construction, calibration, and use of the 10-probe rake can be found in Ref. 16. Five-hole probe measurement uncertainty, determined by the procedure described in Ref. 17, was 0.2 deg for flow angle and 1.0% of dynamic pressure for total pressure (95% confidence).

Surface static pressures inside the S duct were recorded by 220 taps located on axial lines at $\phi = 10$, 90, and 170 deg, as well as circumferential lines at $s/D_1 = 0.96$, 2.97, and 4.01. Surface static pressure measurement uncertainty was 0.3% of dynamic pressure (95% confidence). Visualization of the near-surface duct flow was achieved by a fluorescent oil dot technique. The flow pattern revealed by the oil dots was both photographed under ultraviolet illumination and transferred to paper by placing paper on the duct surface after the test and allowing the paper to absorb the fluorescent oil.

Vortex Generator Array

The wishbone and tapered-fin type vortex generators used in this study are illustrated in Fig. 2. Previous studies[18] indicate that each wishbone generator forms a pair of counter-rotating vortices with the flow between vortices directed upwards, away from the wall. Each tapered-fin vortex generator works in a manner very similar to blade type vortex generators and produces a single trailing axial vortex. Tapered-fin vortex generators may be placed in either co- or counter-rotating arrays. A corotating array results when all

Table 1 Summary of wishbone vortex generator array parameters tested

$l/D_1(N)$	h/D_1, %	s/D_1
0.280 (8)	3.89	1.1, 1.6, 2.1
0.280 (8)	0.62, 1.55, 3.89, 6.22	1.6
0.156 (12), 0.280 (8), 0.404 (6)	3.89	1.6

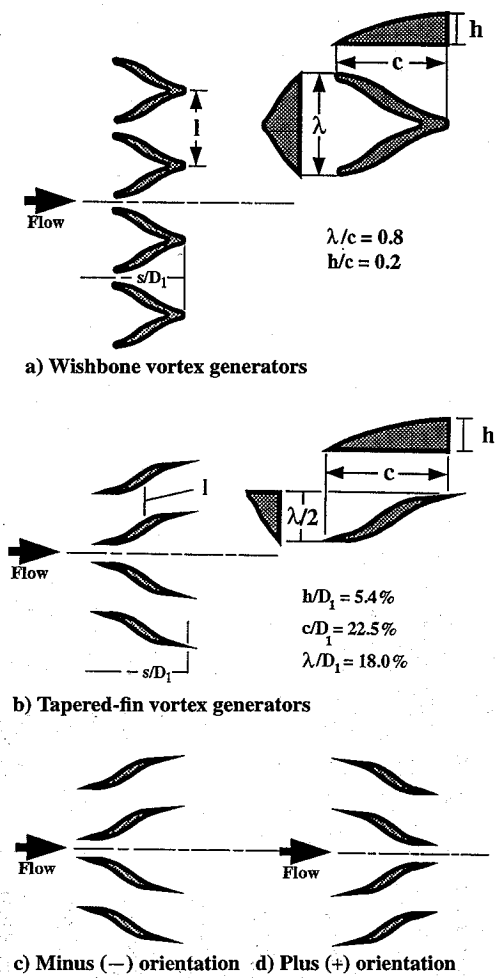

Fig. 2 Vortex generator array geometry.

vortex generators laying in either half of the array have the same orientation (i.e., the vortex generators are placed at the same angle of attack relative to the flowfield). A counter-rotating array exists when pairs of adjacent vortex generators have opposite orientation (i.e., the magnitude of the angle of attack is the same, but the sign is different). The wishbone vortex generator works much like a pair of very closely spaced tapered-fin generators placed in a counter-rotating configuration.

The first series of tests employed single cross-stream arrays of wishbone vortex generators and explored the variation of three parameters: 1) the generator size, which is characterized by the generator height h/D_1, 2) the axial placement of the vortex generator array in the duct s/D_1, and 3) the lateral spacing between the vortex generators l/D_1. The definition of these parameters is illustrated in Fig. 2a. Each parameter was varied while the remaining two parameters were held constant to ascertain their separate effects. The arrays of wishbone vortex generators did not span the full duct circumference, but were contained within the circumferential region $80 < \phi < 280$ deg. By varying the lateral spacing, the number of vortex generators N also changed. The test configuration parameters are summarized in Table 1. A representative location of the vortex generator arrays in the S duct is shown in Fig. 1. The axial placement of the vortex generator arrays was near the origin of separation that occurs in the duct without vortex generators installed ($s/D_1 = 2.02$ at $\phi = 180$ deg), as is indicated in Fig. 1. All vortex generator configurations were placed symmetrically about the line $\phi = 180$ deg (i.e., the symmetry plane of the diffusing S duct) and employed an even number of vortex generators, so that no vortex generator was located at $\phi = 180$ deg. The conventional belief was that the axial vortices produced by the wishbone vortex generators would mix freestream and boundary-layer fluids to re-energize the boundary layer. Re-energization would make the boundary layer less susceptible to cross-stream pressure gradients, thereby eliminating flow separation and reducing the total pressure defect at the duct exit.

Table 2 Summary of tapered-fin vortex generator array parameters tested

N	l/D_1	Orientation
2, 4, 6, 8, 10	0.156	−
4, 6	0.156, 0.500	−
4	0.156	+, −

The studies of tapered-fin vortex generators also utilized single cross-stream arrays, placed in corotating configurations, as shown in Fig. 2b, and explored the variation of three parameters: 1) the number of generators used, 2) the relative spacing between the vortex generators, and 3) the orientation of the array. In each case, the arrays utilized an even number of vortex generators and possessed symmetry with respect to the line $\phi = 180$ deg. Orientation is designated either plus (+) or minus (−). A minus orientation represents a corotating array with vortex generators placed at an angle of attack that directs boundary-layer fluid outward from the array center, as is shown in Fig. 2c. Figure 2d shows a plus orientation that directs boundary-layer fluid inward toward the array center. For the tapered-fin vortex generator configurations the array was not confined to a fixed circumferential region. Rather, for a fixed lateral spacing, a change in the number of vortex generators would also change the circumferential span of the array. The axial location of all tapered-fin vortex generator array tests was $s/D_1 = 1.6$, and the height of the vortex generators was $h/D_1 = 5.4\%$ (or slightly greater than δ_{ref}). The values chosen for tapered-fin vortex generator height and axial location were guided by the results for wishbone vortex generators. Table 2 summarizes all tapered-fin vortex generator test parameters. Instead of attempting to re-energize the boundary layer, in this series of tests we used vortex generators to turn the flow in the boundary layer away from the inside of the first duct bend and suppress the development of secondary flows.

Results and Discussion

Static and total pressure plots are presented as pressure coefficients defined by Eqs. (2) and (3). The pressures p_0 and p represent the local values of total and static pressure. The reference variables, subscripted ref, were evaluated at a location one-half duct diameter upstream of the S-duct inlet ($s/D_1 = -0.5$). The uncertainty of both pressure coefficients was less than 0.015 (95% confidence):

$$Cp = \frac{p - p_{ref}}{p_{0,ref} - p_{ref}} \tag{2}$$

$$Cp_0 = \frac{p_0 - p_{ref}}{p_{0,ref} - p_{ref}} \tag{3}$$

The customary procedure used to calculate total pressure recovery and spatial total pressure distortion[19,20] is based on 40 measured values of total pressure obtained from a standard 40-probe rake. Instead, we used all 720 measurements to determine our total pressure recovery and spatial distortion elements. The total pressure recovery was determined by dividing the area-weighted average total pressure for the exit plane (i.e., the face average total pressure $\overline{p_0}_{,face}$) by the inlet total pressure $p_{0,ref}$. Circumferential and radial total pressure distortion elements were calculated according to the definitions given in Refs. 19 and 20. The circumferential distortion at a radial location is characterized by the intensity $\Delta pc/p$ given by Eq. (4) and the angular extent θ^-. Concepts pertaining to these definitions are illustrated in Fig. 3. Circumferential distortion intensity is a measure of the magnitude of the total pressure defect and angular extent the size of the defect. Radial distortion intensity $\Delta pr/p$

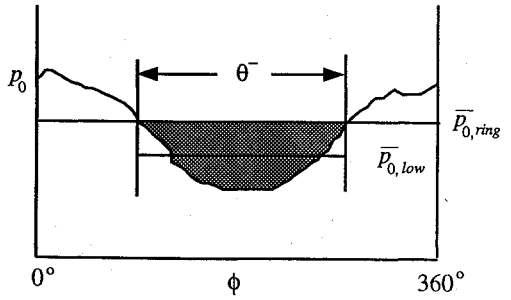

Fig. 3 Concepts used in distortion element definitions.

is defined by Eq. (5). Negative values of radial distortion indicate radial locations where the ring average total pressure exceeds the face average total pressure. Values of the circumferential and radial distortion elements were calculated for measurements recorded at 20 radial locations. Reported here are peak values of the circumferential distortion intensity element and the corresponding extent element for that defect. Maximum and minimum values of the radial distortion element and their corresponding radial locations are also given. Uncertainty of the quantities $\overline{p_{0,\text{face}}}/p_{0,\text{ref}}$, $\Delta pc/p$, and $\Delta pr/p$ were each less than 0.001 (95% confidence),

$$\Delta pc/p = \frac{\overline{p_{0,\text{ring}}} - \overline{p_{0,\text{low}}}}{\overline{p_{0,\text{ring}}}} \tag{4}$$

$$\Delta pr/p = \frac{\overline{p_{0,\text{face}}} - \overline{p_{0,\text{ring}}}}{\overline{p_{0,\text{face}}}} \tag{5}$$

Bare Duct

Figure 4 shows results for flow in the diffusing S duct without vortex generators (i.e., the bare duct). These results serve as a baseline for which to compare results for flow with vortex generators. Figure 4a illustrates surface flow visualization results. The region shown in Fig. 4a approximately corresponds to the area labeled separated flow region in Fig. 1. The flow in Fig. 4a is from left to right. The familiar spiral node associated with three-dimensional separation is readily apparent. Streamline curvature results in a cross-stream static pressure gradient with the lowest static pressure along the inside of the bend (at $\phi = 180$ deg). This initiates fluid motion within the boundary layer toward the inside of the duct bend. Upstream of the flow separation ($s/D_1 = 2.02$) in the angular range between $80 < \phi < 280$ deg the flow is seen converging strongly toward the axial line $\phi = 180$ deg. Continuity forces these converging flows up and away from the duct surface. This motion initiates the naturally occurring pair of counter-rotating vortices observed at the duct exit. At the duct surface along the axial line $\phi = 180$ deg the streamwise adverse pressure gradient is even greater than what results from increasing area alone as the static pressure adjusts to the streamline curvature change between the first and second bends. The converging flow of low momentum fluid near $\phi = 180$ deg reduces the ability of the boundary layer to withstand the enhanced streamwise adverse pressure gradients and flow separation results.

Contours of the total pressure coefficient at the duct exit are shown in Fig. 4b. The large total pressure defect in the lower duct-half represents significant spatial total pressure distortion. This is the phenomena that we are attempting to improve with vortex generators. The total pressure distortion in Fig. 4b results from the naturally occurring vortices convecting low-momentum fluid away from the duct walls. Transverse velocity vectors measured at the duct exit are shown in Fig. 4c, where the pair of naturally occurring vortices is apparent. The length of the reference vector shown below the plot is proportional to one-half the average exit velocity.

Figure 4d shows values of the axial static pressure coefficient and Fig. 4e the circumferential static pressure coefficient for the bare duct. The effect of flow separation can be clearly seen. The constant values of axial static pressure at $2 < s/D_1 < 3$ for the taps at $\phi = 90$ and 170 deg are associated with the flow separation. For unseparated flow the axial static pressure there should be monotonically increasing. The effect of the separated flow is also evident in

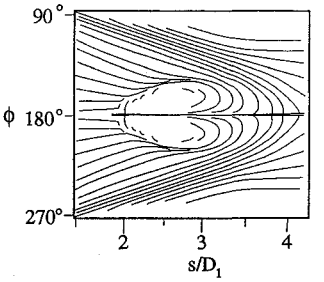

a) Surface flow visualization

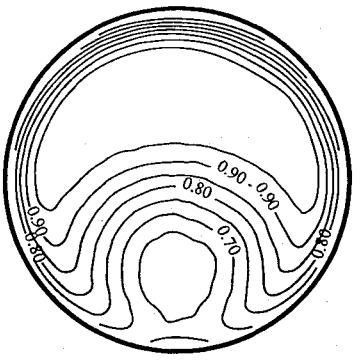

b) Total pressure coefficient

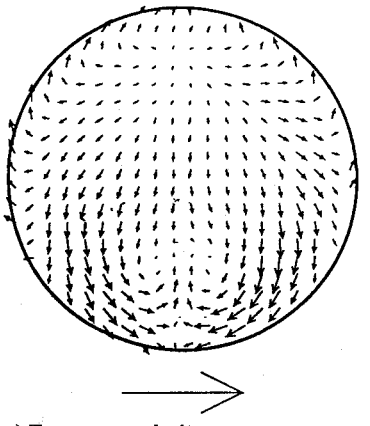

c) Transverse velocity

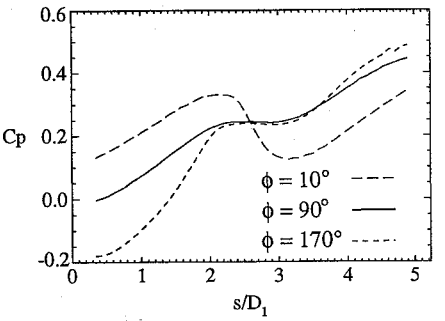

d) Axial static pressure coefficient

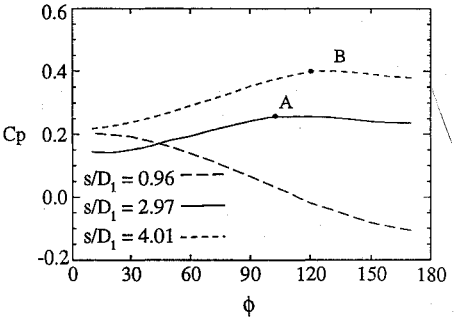

e) Circumferential static pressure coefficient

Fig. 4 Bare duct results.

Table 3 Total pressure recovery and spatial distortion elements for the test conditions in Tables 1 and 2

Vortex generator parameters	$\frac{\overline{p_{0,\text{face}}}}{\overline{p_{0,\text{ref}}}}$,	max, $\Delta pc/p$	θ^-	max, $\Delta pr/p(r/r_2)$	min, $\Delta pr/p(r/r_2)$
		Bare duct			
N.A.	0.968	0.036	136	0.034 (0.97)	−0.010 (0.71)
		Wishbone vortex generators			
$s/D_1 = 1.6, l/D_1 = 0.280,$					
$h/D_1 = 0.62\%$	0.967	0.034	135	0.034 (0.97)	−0.009 (0.71)
$h/D_1 = 1.55\%$	0.969	0.038	122	0.035 (0.97)	−0.011 (0.00)
$h/D_1 = 3.89\%$	0.971	0.037	117	0.033 (0.97)	−0.023 (0.00)
$h/D_1 = 6.22\%$	0.968	0.029	153	0.031 (0.97)	−0.027 (0.00)
$l/D_1 = 0.280, h/D_1 = 3.89\%,$					
$s/D_1 = 1.1$	0.970	0.036	114	0.036 (0.97)	−0.025 (0.00)
$s/D_1 = 1.6$	0.971	0.037	117	0.033 (0.97)	−0.023 (0.00)
$s/D_1 = 2.1$	0.968	0.033	128	0.034 (0.97)	−0.008 (0.66)
$s/D_1 = 1.6, h/D_1 = 3.89\%,$					
$l/D_1 = 0.404$	0.968	0.037	125	0.033 (0.97)	−0.019 (0.00)
$l/D_1 = 0.280$	0.971	0.037	117	0.033 (0.97)	−0.023 (0.00)
$l/D_1 = 0.156$	0.969	0.046	105	0.038 (0.97)	−0.026 (0.00)
		Tapered-fin vortex generators			
$l/D_1 = 0.156$, orientation = −,					
$N = 2$	0.976	0.032	143	0.031 (0.97)	−0.022 (0.00)
$N = 4$	0.974	0.024	175	0.026 (0.97)	−0.021 (0.00)
$N = 6$	0.973	0.022	95	0.022 (0.97)	−0.024 (0.00)
$N = 8$	0.972	0.024	79	0.022 (0.97)	−0.025 (0.00)
$N = 10$	0.971	0.029	66	0.023 (0.97)	−0.030 (0.00)
Orientation = −, $N = 2$,					
$l/D_1 = 0.156$	0.974	0.024	175	0.026 (0.97)	−0.021 (0.00)
$l/D_1 = 0.500$	0.975	0.017	100	0.029 (0.97)	−0.025 (0.05)
Orientation = −, $N = 4$,					
$l/D_1 = 0.156$	0.973	0.022	95	0.022 (0.97)	−0.024 (0.00)
$l/D_1 = 0.500$	0.973	0.019	59	0.028 (0.97)	−0.028 (0.00)
$N = 4, l/D_1 = 0.156,$					
Orientation = +	0.974	0.024	175	0.026 (0.97)	−0.021 (0.00)
Orientation = −	0.971	0.028	160	0.036 (0.00)	−0.018 (0.76)

the circumferential static pressure at $s/D_1 = 2.97$ and 4.01, which lie within the region of separated flow. Peak values of static pressure were observed at $\phi = 100$ deg for taps at $s/D_1 = 2.97$ (labeled point A) and $\phi = 120$ deg at $s/D_1 = 4.01$ (labeled point B). For unseparated flow the static pressure there should increase monotonically with the maximum static pressure at $\phi = 180$ deg.

Values of total pressure recovery and spatial distortion elements are given in Table 3. Note that the minimum value of $\Delta pr/p$ (hence, the maximum ring average total pressure) occurs at $r/r_2 = 0.71$, quite a distance from the duct center. This is caused by the large total pressure defect that extends to the duct center.

Wishbone Vortex Generator Arrays

Figure 5 compares results for two different values of vortex generator height, $h/D_1 = 1.55\%$ and 6.22%. The axial location and lateral spacing remained constant. The results in Fig. 5a show significantly higher values of the axial static pressure coefficient for flow with vortex generators (black lines) in the region $2 < s/D_1 < 4$, particularly for the larger array. The static pressure values for the smaller vortex generators nearly return to the levels without vortex generators (gray lines) at $s/D_1 > 4$; whereas for the larger vortex generators, the static pressure values remain considerably higher than the values for flow without vortex generators. This would suggest that the smallest configuration of vortex generators is reducing the separated flow region but is having little effect on the flow at the duct exit, whereas the larger generators are, to some extent, also affecting the flow at the duct exit.

Contours of the total pressure coefficient at the duct exit are shown in Fig. 5b. The smallest vortex generators have only slightly reduced the total pressure defect when compared to the bare duct results. The shape of the contours remains the same, but the total pressure contour levels appear approximately 0.05 higher for flow with vortex

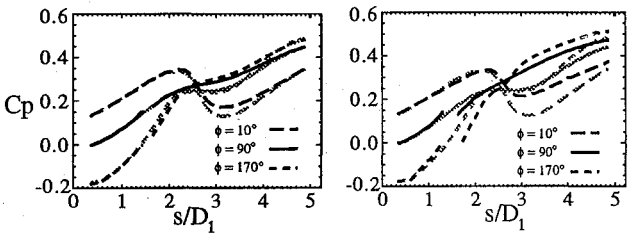

a) Axial static pressure coefficient

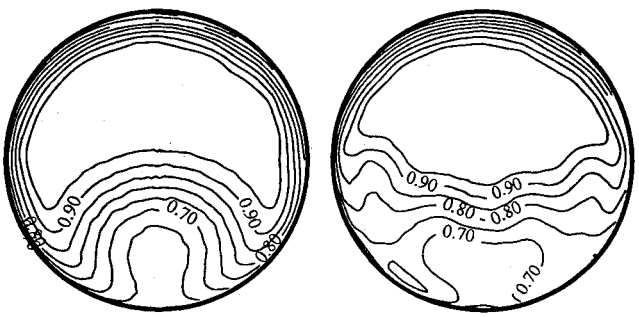

b) Total pressure coefficient

Fig. 5 Variation in height of wishbone vortex generators; h/D_1 = 1.55% left, h/D_1 = 6.22% right.

generators. For the larger vortex generators the shape of the total pressure defect appears to be significantly altered when compared to the bare duct (Fig. 4b).

Table 3 contains values of the total pressure recovery and spatial distortion elements. Two other vortex generator heights were also tested, $h/D_1 = 0.62\%$ and 3.9%. The greatest total pressure recovery improvement resulted from the array with vortex generator

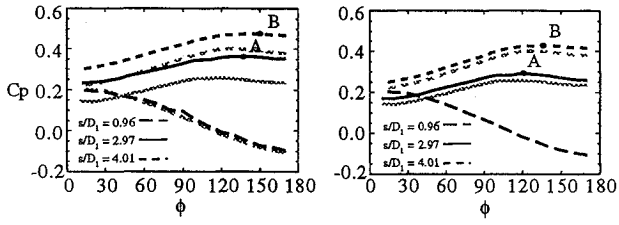

a) Circumferential static pressure coefficient

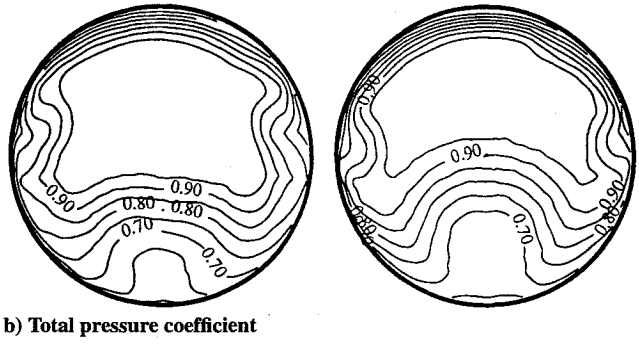

b) Total pressure coefficient

Fig. 6 Variation in axial location of wishbone vortex generators; s/D_1 = 1.1 left, s/D_1 = 2.1 right.

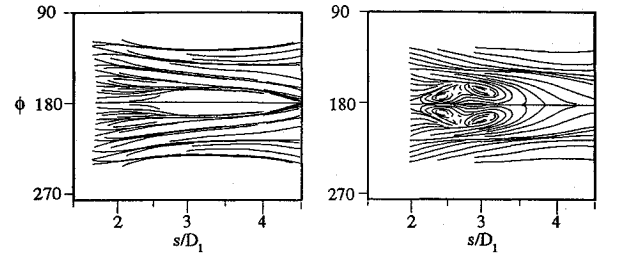

a) Surface flow visualization

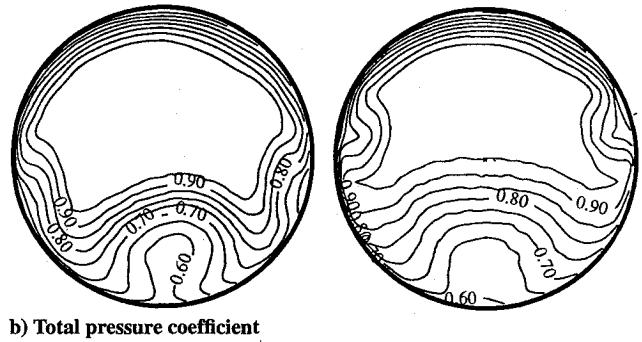

b) Total pressure coefficient

Fig. 7 Variation in lateral spacing of wishbone vortex generators; l/D_1 = 1.56 left, l/D_1 = 0.404 right.

heights of $h/D_1 = 3.9\%$. Radial distortion was improved by all arrays except the smallest, where the minimum value of $\Delta pr/p$ still occurs at $r/r_2 = 0.71$. The only significant improvement in circumferential distortion was affected by the largest vortex generator array configuration. It appears that the greatest improvement in total pressure recovery and spatial distortion is obtained when the vortex generator height is roughly equal to or slightly greater than the inlet boundary-layer thickness.

Figure 6 compares results for vortex generator arrays at two different axial locations, $s/D_1 = 1.1$ and 2.1. The vortex generator height and lateral spacing remained unchanged. As the axial location of the vortex generator array approaches the separation point for flow without vortex generators ($s/D_1 = 2.02$) any beneficial effect of the vortex generator array diminishes rapidly. This is particularly noticeable in the circumferential static pressure coefficient plots, Fig. 6a. Little difference exists between the flow with vortex generators (black lines) at axial location of $s/D_1 = 2.1$ and the flow without vortex generators (gray lines). The array located at $s/D_1 = 1.1$ produces a flow with static pressure markedly higher than exists in the flow without vortex generators, particularly in the separated flow region. The location of the peak values of static pressure in Fig. 6a, points A and B, indicate that the array at $s/D_1 = 1.1$ is reducing the circumferential span of the separated region at $s/D_1 = 2.97$ and 4.01.

Total pressure coefficient contours shown in Fig. 6b for vortex generator arrays installed at $s/D_1 = 1.1$ show the distance that the total pressure defect extends away from the wall in the lower duct-half has been reduced compared to flow without vortex generators. This is not the case for vortex generators at $s/D_1 = 2.1$ where the total pressure defect is comparable to flow without vortex generators.

Results in Table 3 show both cases yield higher total pressure recovery with the array at $s/D_1 = 1.1$ producing the most significant improvement. An additional axial location, $s/D_1 = 1.6$, was also tested that yielded the highest value of total pressure recovery. None of the three axial locations significantly lowered circumferential distortion below the level without vortex generators. Radial distortion was improved, however, for vortex generator arrays at $s/D_1 = 1.1$ and 1.6. The results suggest that as a guideline it appears that the location of the vortex generator array should be moderately upstream of the separation.

For the results presented in Fig. 7, only the lateral spacing between vortex generators within the array was varied while their height and axial location remained fixed. The two values of lateral spacing shown in Fig. 7 are $l/D_1 = 0.156$ and 0.404. From the surface flow visualization shown in Fig. 7a, it appears that the configuration with the closest spacing of vortex generators $l/D_1 = 0.156$ is the most effective in reducing flow separation. The widely spaced vortex generator test case, $l/D_1 = 0.404$, does not significantly reduce the size of the separated flow region. In all cases the separation lies within the streamlines trailing behind the center pair of vortex generators.

Contours of the total pressure coefficient are shown in Fig. 7b. Despite the large difference in the vortex generator spacing and the disparity observed in the flow visualization results, the total pressure contours are relatively similar. The results in Table 3 indicate that the wishbone vortex generator arrays are producing modest improvements in total pressure recovery and radial distortion but are ineffective in improving circumferential distortion.

Tapered-Fin Vortex Generator Arrays

Figure 8 shows results for two different tapered-fin vortex generators arrays. Each array used vortex generators that are identical in size, axial location, orientation, and lateral spacing, but differed in the number of vortex generators used. The results in Fig. 8 are for arrays of two and eight tapered-fin vortex generators. In Fig. 8a both arrays produced significantly higher values of the axial static pressure coefficient than either the bare duct or any array of wishbone vortex generators tested.

Regarding the transverse velocity, Fig. 8b, with two vortex generators the strength of the naturally occurring vortices is reduced, and they are displaced outward, away from $\phi = 180$ deg when compared to bare duct results. The naturally occurring vortices are no longer observed when eight vortex generators are used. The transverse velocity components are quite large, and the entire exit flowfield is dominated by two vortices that rotate in a direction opposite to that of the naturally occurring vortices.

Observing contours of the total pressure coefficient in Fig. 8c, with two vortex generators the region of low-momentum flow is displaced toward either side of the duct in two distinct regions. With eight vortex generators, the boundary layer is now thinnest along the bottom surface of the duct, at the same location where the naturally occurring vortices were responsible for the large region of low-momentum flow in the absence of vortex generators. This indicates that the secondary flow generated by the vortex generators overwhelm the natural secondary flow.

Three other configuration were also tested ($N = 4$, 6, and 10) and the total pressure recovery and spatial distortion elements are summarized in Table 3. In general, the total pressure recovery observed was greater than any array of wishbone vortex generators.

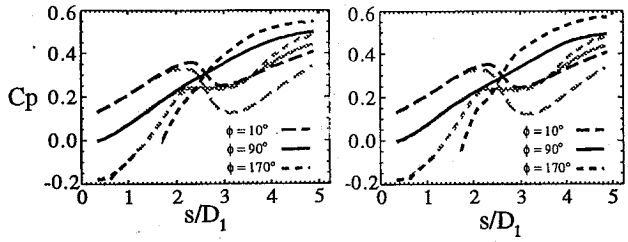

a) Axial static pressure coefficient

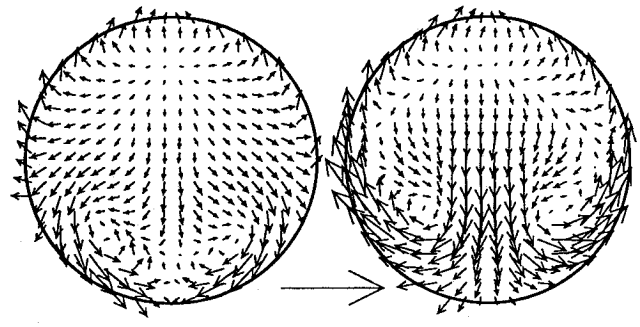

b) Transverse velocity

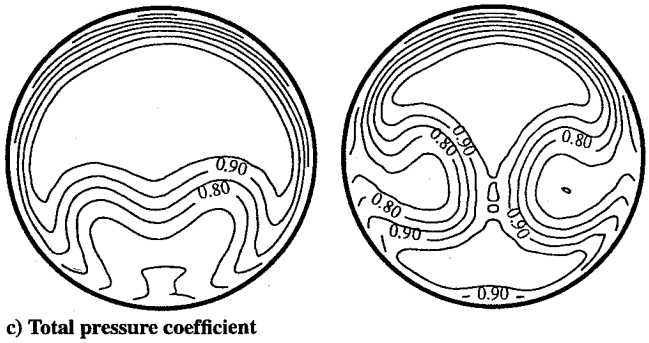

c) Total pressure coefficient

Fig. 8 Variation in number of tapered-fin vortex generators; $N = 2$ left, $N = 8$ right.

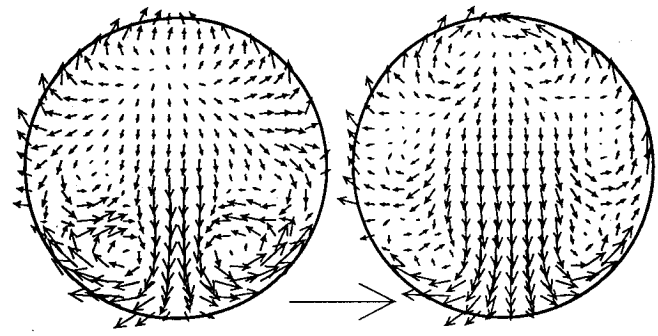

a) Transverse velocity

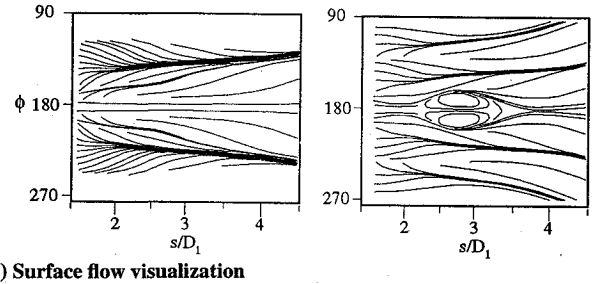

b) Surface flow visualization

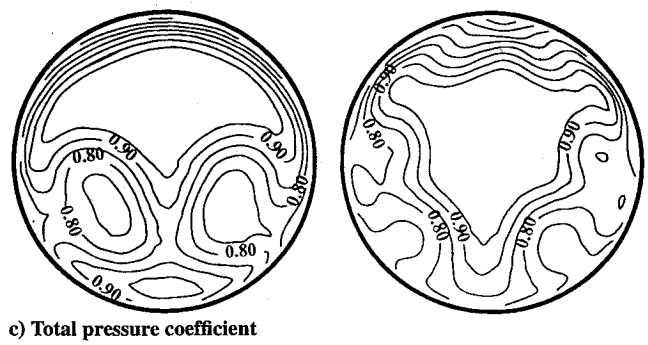

c) Total pressure coefficient

Fig. 9 Variation in lateral spacing of tapered-fin vortex generators; $l/D_1 = 0.156$ left, $l/D_1 = 0.500$ right.

The configuration with two vortex generators produced the highest total pressure recovery, and the total pressure recovery decreased with each additional pair of vortex generators. Circumferential and radial distortion were also significantly improved, with the least circumferential distortion resulting from the array which used six vortex generators.

The next results compare a change in vortex generator lateral spacing. Each array used six identically sized tapered-fin vortex generators placed at the same axial location. Figure 9 displays results for two values of lateral spacing, a narrow-spaced configuration ($l/D_1 = 0.156$) and a wide-spaced configuration ($l/D_1 = 0.500$).

The transverse velocity results in Fig. 9a show a significant difference results from change in vortex generator lateral spacing. For the wide-spaced vortex generator array, the naturally occurring vortices are barely discernible; whereas for the narrow-spaced vortex generator array, the naturally occurring vortices are easily identified. Individual vortices from each vortex generator are observed for the wide-spaced vortex generator array, whereas the narrow-spaced vortex generator array appears to create a single pair of vortices.

Figure 9b shows flow visualization results. In both drawings the flow is from left to right. Because of the wide spacing, the flow pattern developed by the outermost vortex generators in Fig. 9b lies outside the region shown in the drawing. The flow separation is absent for the narrow-spaced vortex generator configurations, whereas Fig. 9b clearly indicates that the wide-spaced vortex generator configuration did not eliminate flow separation. Comparison with bare duct results shows that the extent of separation is reduced.

For the wide-spaced configurations, on the right side of Fig. 9c, it appears that the total pressure defect is more evenly distributed along the duct surface when compared to the narrow-spaced configuration. Table 3 shows that this represents an improvement in circumferential total pressure distortion. Table 3 also contains results for another comparison of vortex generator lateral spacing that used four vortex generators. There is almost no difference in total pressure recovery between the wide- and narrow-spaced configurations. This result is particularly interesting since the narrow-spaced configurations eliminated separation, whereas the wide-spaced configurations did not.

The most persuasive data to support our hypothesis regarding the fluid mechanics responsible for the beneficial effect that vortex generators produce in the diffusing S duct are obtained by comparing arrays that are identical in every respect except the vortex generator orientation. Figure 10 shows exit plane survey results for two different arrays composed of four narrow-spaced tapered-fin vortex generators in corotating configurations. The two configurations differ only in their orientation. One array, shown on the left side of Fig. 10, is oriented to oppose the local secondary flow (− orientation), whereas the orientation of the other configuration, shown on the right side of Fig. 10, would enhance the local secondary flow (+ orientation).

If mixing was responsible for improved aerodynamic performance, then both configurations should have effects that are approximately equal. If, however, the improved aerodynamic performance results from suppressing the naturally occurring vortices by turning the flow, then the first array should improve aerodynamic performance while the second array should worsen performance. The latter effect is, in fact, what happens. This is clearly seen in Fig. 10. For the positive orientation, Fig. 10a shows the naturally occurring vortices are strengthened, and Fig. 10b shows the total pressure defect is even more pronounced when compared to the bare duct. In fact, the total pressure defect lies nearly at the duct

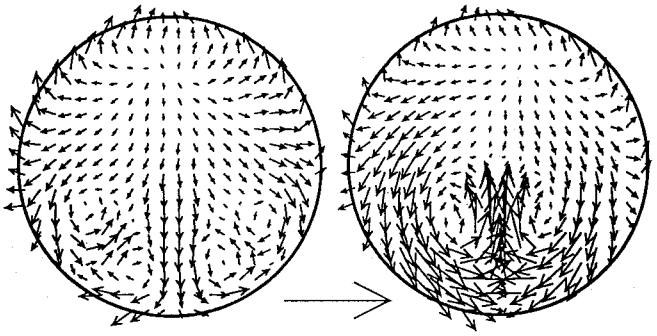

a) Transverse velocity

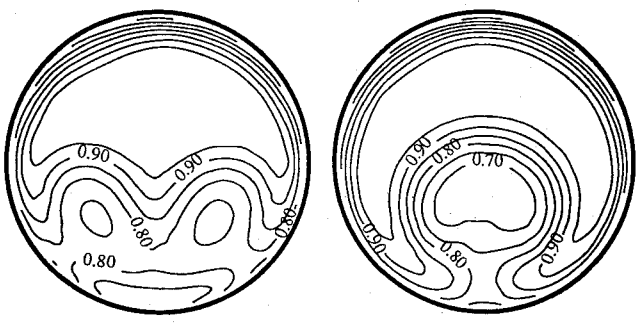

b) Total pressure coefficient

Fig. 10 Variation in orientation of tapered-fin vortex generators; minus left, plus right.

center, resulting in an apparent improvement in circumferential distortion, given in Table 3, when compared to the bare duct. However, the radial distortion has greatly deteriorated, so that the maximum value of $\Delta pr/p$ is at the duct center, and the minimum value of $\Delta pr/p$ lies relatively near the duct surface.

Summary

Two series of experiments were conducted to use vortex generators arrays to improve the aerodynamic performance (as measured by total pressure recovery and spatial distortion) of a diffusing S duct. The first series of tests used wishbone vortex generators and explored the variation of vortex generator height, axial location, and lateral spacing. Modest improvements in total pressure recovery and radial distortion were obtained; however, no array of wishbone vortex generators was successful at significantly improving circumferential total pressure distortion or eliminating flow separation. A second series of test were conducted using tapered-fin vortex generators. The number of vortex generators, their lateral spacing, and their orientation were varied. Results from the second test series showed significant improvements in all elements of aerodynamic performance when compared to the bare duct results or the first series test results.

From the tests we concluded that most of the degraded aerodynamic performance results from secondary flow, initiated by streamline curvature, producing a pair of naturally occurring vortices that convect low-momentum fluid into the midpassage region of the duct. This produces a significant total pressure defect at the duct exit. This total pressure defect has been observed in S ducts with and without flow separation. In the second series of tests, we used the vortex generators to control the development of secondary flow by turning the boundary layer away from the inside of the first duct bend to suppress the naturally occurring vortices. Our results do not imply that vortex generators do not effect boundary-layer reenergization; there are excellent studies of two-dimensional and axisymmetric diffusers that have established this fact. For internal, three-dimensional flows, however, we believe that greater aerodynamic performance improvement will be obtained by using vortex generators to control the development of secondary flows by redirecting the flow rather than relying on mixing to re-energize the boundary layer.

Acknowledgments

We are grateful for the assistance and insight provided by W. Darby, R. Davis, P. D. Eastman, R. Gronski, W. Hingst, D. Hwang, A. Porro, S. Wellborn, and K. Zaman.

References

[1]Vakili, A. D., Wu, J. M., Liver, P., and Bhat, M. K., "Experimental Investigation of Secondary Flows in a Diffusing S-Duct," Univ. of Tennessee Space Inst., TR UTSI 86/14, Univ. of Tennessee, Tullahoma, TN, Sept. 1984.

[2]Wellborn, S. R., Reichert, B. A., and Okiishi, T. H., "An Experimental Investigation of the Flow in a Diffusing S-Duct," AIAA Paper 92-3622, July 1992; also NASA TM 105809, Aug. 1992.

[3]Tobak, M., and Peake, D. J., "Topology of Three-Dimensional Separated Flows," *Annual Review of Fluid Mechanics*, Vol. 14, 1982, pp. 61–85.

[4]Chapman, G. T., and Yates, L. A., "Topology of Flow Separation on Three-Dimensional Bodies," *Applied Mechanics Reviews*, Vol. 44, July 1991, pp. 329–345.

[5]Vakili, A., Wu, J. M., Liver, P., and Bhat, M. K., "Measurements of Compressible Secondary Flow in a Circular S-Duct," AIAA Paper 83-1739, July 1983.

[6]Kline, S. J., Abbott, D. E., and Fox, R. W., "Optimum Design of Straight Walled Diffusers," *Journal of Basic Engineering*, Vol. 81, No. 3, 1959, pp. 305–320.

[7]Taylor, H. D., "Retractable Vortex Generators," United Aircraft Corp. Research Dept., Rept. M-15355-3, East Hartford, CT, June 1950.

[8]Brown, A. C., "Subsonic Diffusers Designed Integrally with Vortex Generators," *Journal of Aircraft*, Vol. 5, 1968, pp. 221–229.

[9]Mitchell, G. A., and Davis, R. W., "Performance of Centerbody Vortex Generators in an Axisymmetric Mixed Compression Inlet at Mach Numbers from 2.0 to 3.0," NASA TN D-4675, July 1968.

[10]Kaldschmidt, G., Syltebo, B. E., and Ting, C. T., "A 727 Airplane Center Duct Inlet Low Speed Performance Confirmation Model Test for Refanned JT8D Engines, Phase 2," NASA CR 134534, Feb. 1973.

[11]Vakili, A. D., Wu, J. M., Liver, P., and Bhat, M. K., "Experimental Investigation of Secondary Flows in a Diffusing S-Duct with Vortex Generators," Univ. of Tennessee Space Inst., Preliminary Copy Final Rept. NASA Contract NAG3 233, July 1986.

[12]Weng, P. F., and Guo, R. W., "New Method of Swirl Control in a Diffusing S-Duct," *AIAA Journal*, Vol. 30, No. 7, 1992, pp. 1918, 1919.

[13]Reichert, B. A., and Wendt, B. J., "An Experimental Investigation of S-Duct Flow Control Using Arrays of Low Profile Vortex Generators," AIAA Paper 93-0018, Jan. 1993; also NASA TM 106030, Feb. 1993.

[14]Reichert, B. A., and Wendt, B. J., "Improving Diffusing S-Duct Performance by Secondary Flow Control," AIAA Paper 94-0365, Jan. 1994; also NASA TM 106492, Feb. 1994.

[15]Porro, A. R., Hingst, W. R., Wasserbauer, C. A., and Andrews, T. B., "The NASA Lewis Research Center Internal Fluid Mechanics Facility," NASA TM 105187, Sept. 1991.

[16]Wendt, B. J., and Reichert, B. A., "A New Algorithm for Five-Hole Probe Calibration and Data Reduction and its Application to a Rake-Type Probe," *Fluid Measurement and Instrumentation Forum—1993*, edited by R. Gore, T. Morrow, and G. Jones, American Society of Mechanical Engineers, New York, 1993, pp. 29–35.

[17]Reichert, B. A., and Wendt, B. J., "Uncertainty of Five-Hole Probe Measurements," *Fluid Measurement and Instrumentation—1994*, edited by T. B. Morrow, G. L. Morrison, and R. A. Gore, American Society of Mechanical Engineers, New York, 1994, pp. 39–44.

[18]Wendt, B. J., and Hingst, W. R., "Measurements and Modeling of the Flow Structure in the Wake of a Low Profile 'Wishbone' Vortex Generator," AIAA Paper 94-0620, Jan. 1994; also NASA TM 106468, Jan. 1994.

[19]Anon., "Gas Turbine Engine Inlet Flow Distortion Guidelines," Society of Automotive Engineers, SAE ARP—1420, March 1978.

[20]Anon., "Inlet Total-Pressure-Distortion Considerations for Gas-Turbine Engines," Society of Automotive Engineers, SAE AIR—1419, May 1978.